Front. Mech. Eng. 2021, 16(1): 46–60
https://doi.org/10.1007/s11465-020-0606-2

RESEARCH ARTICLE

Hui YANG, Hairong FANG, Yuefa FANG, Xiangyun LI

Dimensional synthesis of a novel 5-DOF reconfigurable hybrid perfusion manipulator for large-scale spherical honeycomb perfusion

Abstract A novel hybrid perfusion manipulator (HPM) with five degrees of freedom (DOFs) is introduced by combining the 5PUS-PRPU (P, R, U, and S represent prismatic, revolute, universal, and spherical joint, respectively) parallel mechanism with the 5PRR reconfigurable base to enhance the perfusion efficiency of the large-scale spherical honeycomb thermal protection layer. This study mainly presents the dimensional synthesis of the proposed HPM. First, the inverse kinematics, including the analytic expression of the rotation angles of the U joint in the PUS limb, is obtained, and mobility analysis is conducted based on screw theory. The Jacobian matrix of 5PUS-PRPU is also determined with screw theory and used for the establishment of the objective function. Second, a global and comprehensive objective function (GCOF) is proposed to represent the Jacobian matrix's condition number. With the genetic algorithm, dimensional synthesis is conducted by minimizing GCOF subject to the given variable constraints. The values of the designed variables corresponding to different configurations of the reconfigurable base are then obtained. Lastly, the optimal structure parameters of the proposed 5-DOF HPM are determined. Results show that the HPM with the optimized parameters has an enlarged orientation workspace, and the maximum angle of the reconfigurable base is decreased, which is conducive to improving the overall stiffness of HPM.

Keywords 5-DOF hybrid manipulator, reconfigurable base, large workspace, dimensional synthesis, optimal design

Received April 3, 2020; accepted August 8, 2020

Hui YANG, Hairong FANG (✉), Yuefa FANG
School of Mechanical Engineering, Beijing Jiaotong University, Beijing 100044, China
E-mail: hrfang@bjtu.edu.cn

Xiangyun LI
School of Mechanical Engineering, Southwest Jiaotong University, Chengdu 610031, China

1 Introduction

With the unceasing development of space activities, many countries have focused on spacecraft research in recent years. However, re-entering spacecraft suffers from the intense aerodynamic heating effect, which influences the normal operation of the equipment and the safety of pilots [1–3]. Therefore, the thermal protection system should be designed in a way that ensures spacecraft safety, which is usually implemented through the perfusion of a heat-resistant material into the thermal protection layer [4]. At present, such perfusion is accomplished manually, which entails low efficiency. An automatic perfusion manipulator should be introduced into the perfusion system to improve perfusion efficiency. The parallel manipulator has elicited much more attention from researchers and manufacturers compared with its serial counterparts in recent years because of its advantages, such as high precision, high dynamic capabilities, and low inertia [5–7]. Owing to these merits, parallel manipulators are widely used in flight simulators [8,9], high-speed pick-and-place robots [10,11], spray painting robots [12,13], and aircraft component machining [14,15]. However, the small workspace and the singular points in the workspace of parallel manipulators hinder their application in the machining of large-scale workpieces. For thermal protection system perfusion, a perfusion manipulator should have a large workspace because of the large size of the perfusion target. Moreover, because the heavy perfusion device is attached to the moving platform, the hybrid perfusion manipulator (HPM) should have high stiffness. Evidently, a serial or parallel manipulator cannot meet perfusion requirements. In this study, a 5-degree-of-freedom (5-DOF) reconfigurable HPM with a large workspace and high stiffness is introduced. Its structural design and kinematics have been studied in Ref. [16].

Aside from kinematics analysis, dimensional design is another important aspect in ensuring the good kinematic performance of hybrid manipulators. The primary issues in dimensional synthesis are defining the appropriate performance indices, reducing the number of optimization variables, and selecting efficient optimization algorithms. Performance chart [17,18] and objective function [19,20] methods are used for the dimensional synthesis of parallel manipulators. Liu and Wang [21] proposed a performance chart for serial or parallel manipulators in which the number of linear parameters is fewer than five. Wang et al. [22] established the relationship between the optimization objectives and kinematic parameters of the 3-PUU (P and U represent prismatic and universal joint, respectively) parallel mechanism by using the performance chart method. Kelaiaia et al. [23] proposed a methodology of dimensional design for a linear Delta parallel robot by utilizing the multi-objective optimization genetic algorithm (GA). To overcome the local optimum, Wan et al. [24] introduced a mutation of GA into particle swarm optimization (MPSO) and performed dimensional optimization on the proposed 8-SPU (S: Spherical joint) parallel manipulator, which can serve as a unit of the support fixture. Altuzarra et al. [25] implemented a dimension design for a symmetric parallel manipulator by using the Pareto front with three performance criteria, namely, dexterity, energy, and workspace volume. Wu et al. [26] investigated the optimal design for a 2-DOF actuation-redundant parallel mechanism in consideration of kinematics and natural frequency. The optimal design of the 4-RSR&SS (R: Revolute joint) parallel tracking mechanism was examined by Qi et al. [27] in consideration of parameter uncertainty and on the basis of the particle swarm algorithm. Klein et al. [28] optimized the torque capabilities of the robotic arm exoskeleton with independent objective functions by modifying the critical kinematic parameters. Song et al. [29] implemented an optimal design of the T5 parallel mechanism by using the NSGA-II method in consideration of engineering requirements. A small-sized parallel bionic eye mechanism was designed by Cheng and Yu [30], and the optimal design based on NSGA-II was applied in consideration of the overall dimensions. To obtain optimal kinematic performance, Daneshmand et al. [31] optimized a spherical manipulator in accordance with the concept of GA. Gosselin and Angeles [32] introduced a global index (GCI) based on the Jacobian matrix's condition number that can be used to evaluate the distribution of the parallel manipulator's global dexterity over the entire workspace. By minimizing the integrated objective function, Huang et al. [33] studied the dimensional synthesis of a 3-DOF manipulator, which is the parallel module of the 5-DOF TriVariant. This method has also been applied to the dimensional synthesis of many other parallel manipulators proposed in Refs. [34,35].

Although researchers have conducted many studies on dimensional optimal design, the majority of them focused on serial or parallel manipulators. Only a few studies have been conducted on the optimization of the 5-DOF hybrid manipulator. Existing studies on the optimal design of the 5-DOF hybrid manipulator concentrated on the parallel module of the manipulator and failed to achieve the comprehensive optimal design of all kinematic parameters. To address this gap, our study proposes global design variables, which combine the parameters of the reconfigurable base, 5PUS-PRPU parallel manipulator, and the task workspace. Dimensional synthesis of the 5-DOF HPM is conducted with the objective function proposed in Refs. [33–35] and GA.

The rest of this paper is arranged into sections. Section 2 briefly introduces the structure of the proposed HPM. The kinematics analysis, including mobility, inverse kinematics, and motion analyses of the U joint in the PUS limb, is presented in Section 3. Section 4 presents the Jacobian matrix in accordance with screw theory, and Section 5 introduces the dimensional synthesis conducted with GA. The conclusions are given in Section 6.

2 Description of the 5-DOF HPM

Figure 1 shows the virtual prototype of the perfusion system, which mainly consists of a 5-DOF HPM, a perfusion device, and a gantry guide rail. Given that the structural features and kinematics of the 5-DOF HPM have been analyzed thoroughly in Ref. [16], this section simply introduces the architecture of the proposed manipulator to facilitate a subsequent analysis.

Figure 2(a) presents the CAD models of the 5-DOF HPM, which is constructed by combining a 1-DOF 5PRR parallel manipulator (Fig. 2(b)) with a 5-DOF 5PUS-PRPU parallel manipulator (Fig. 2(c)) in series. In accordance with the design concept of the proposed hybrid manipulator, the 5PRR parallel manipulator is fixed during the perfusion of the 5-DOF 5PUS-PRPU parallel manipulator and can be regarded as the base of the 5PUS-PRPU parallel manipulator. The structure of the 5PRR parallel mechanism changes as the angle θ changes, which indicates that the base of the 5PUS-PRPU parallel manipulator is changeable. Thus, reconfigurability of the hybrid manipulator is realized. Figure 2(d) shows a diagram of the proposed HPM. B-$x_\mathrm{b}y_\mathrm{b}z_\mathrm{b}$ and P-$x_\mathrm{p}y_\mathrm{p}z_\mathrm{p}$ denote fixed and moving frames, which are parallel to each other in the initial position. For the ith PRR branch, A_i denotes the P joint and the first R joint, and B_i denotes the second R joint. The x_b axis is coincident with the vector $\overrightarrow{BA_1}$, the z_b axis is perpendicular to the base plane, and the y_b axis conforms to the right-hand rule. For the ith PUS limb, the P and U joints and the S joint are represented by C_i and D_i, respectively. A_6 and B_6 denote the first P and R and the second P of the

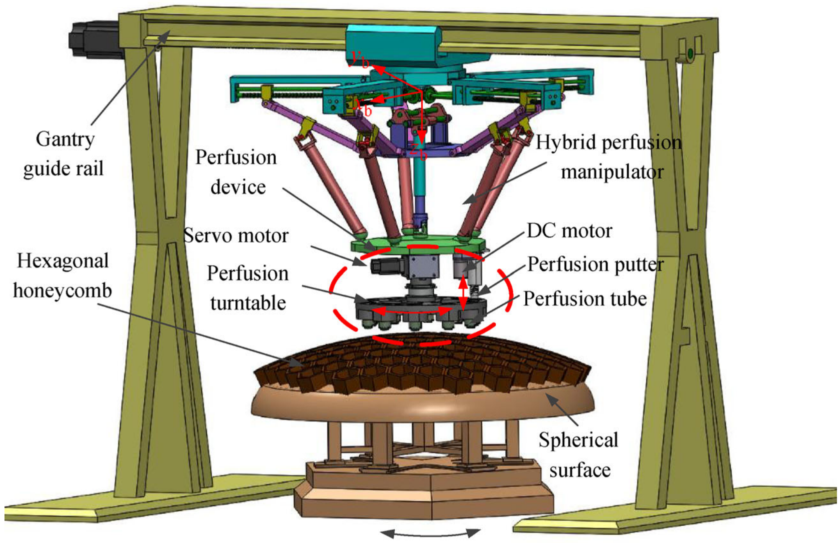

Fig. 1 Virtual prototype of the perfusion system. DC: Direct current.

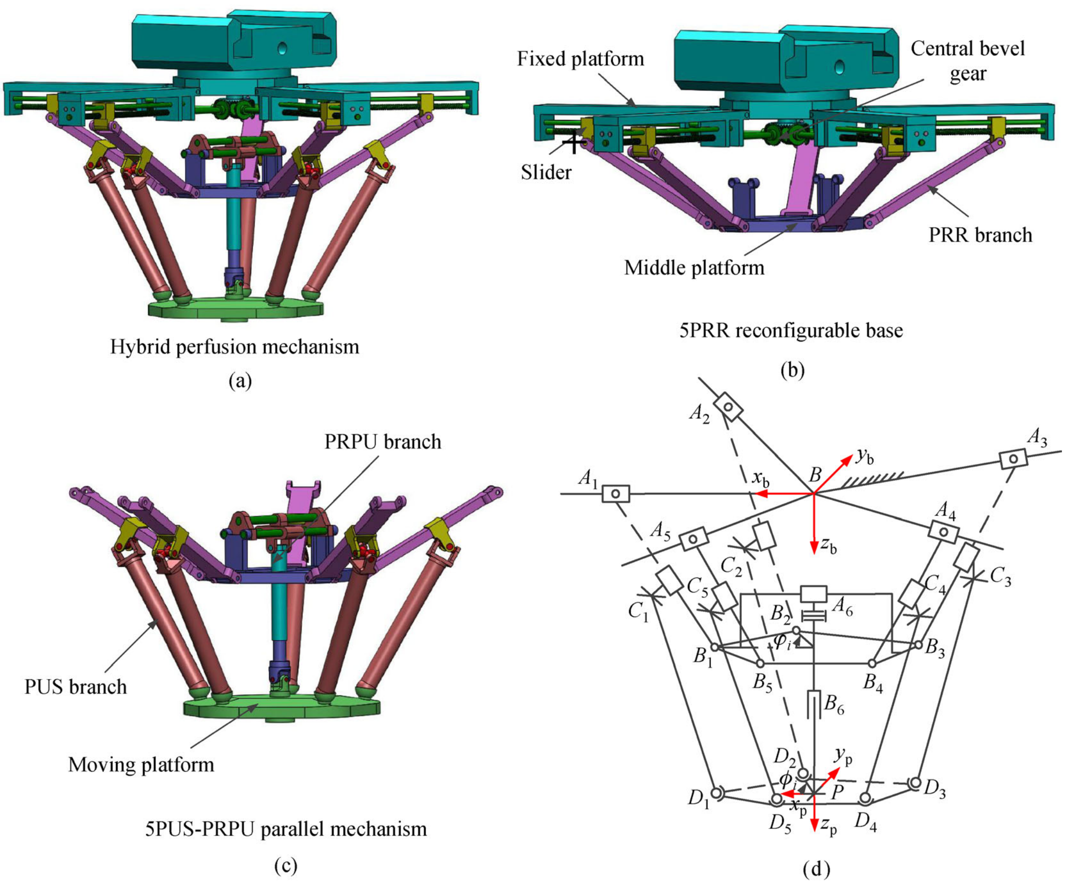

Fig. 2 Structure model and kinematic diagram of the hybrid perfusion mechanism: (a) Hybrid perfusion mechanism, (b) 5PRR reconfigurable base, (c) 5PUS-PRPU parallel mechanism, and (d) kinematic diagram.

middle passive PRPU limb, respectively. The angles measured from the x_b axis to $\overrightarrow{BA_i}$ and from the x_p axis to $\overrightarrow{PD_i}$ are represented by φ_i and ϕ_i, respectively.

3 Kinematics

3.1 Mobility analysis

The proposed HPM consists of the 5PRR parallel mechanism and the 5PUS-PRPU parallel manipulator. The reconfigurable base has one translational DOF along the z_b axis. The PUS limb has six DOFs, indicating that it provides no constraint on the moving platform. Thus, this section focuses on the mobility analysis of the PRPU limb by using screw theory [36].

Figure 3 shows the twist system of the PRPU limb. The unit screw $\$_i = [\boldsymbol{s}; \boldsymbol{s}_0]^{\mathrm{T}}$ is used to represent the screw coordinates of the ith joint. $\boldsymbol{s}$ denotes a unit vector pointing in the direction of the screw axis, $\boldsymbol{s}_0 = \boldsymbol{r} \times \boldsymbol{s}$ defines the moment of the screw axis about the origin of the B-$x_by_bz_b$ frame, and $\boldsymbol{r}$ represents the position vector of any point on the screw axis with respect to the B-$x_by_bz_b$ frame. For a prism, unit screw $\$_i$ is equal to $[0 \quad 0 \quad 0; \boldsymbol{s}]^{\mathrm{T}}$. The PRPU limb's twist system can be presented as

$$\begin{cases} \$_1 = [0 \quad 0 \quad 0; \quad 0 \quad 1 \quad 0]^{\mathrm{T}}, \\ \$_2 = [0 \quad 1 \quad 0; \quad 0 \quad 0 \quad 0]^{\mathrm{T}}, \\ \$_3 = [0 \quad 0 \quad 0; \quad l_3 \quad 0 \quad m_3]^{\mathrm{T}}, \\ \$_4 = [0 \quad 1 \quad 0; \quad p_4 \quad 0 \quad q_4]^{\mathrm{T}}, \\ \$_5 = [l_5 \quad 0 \quad m_5; \quad p_5 \quad q_5 \quad r_5]^{\mathrm{T}}, \end{cases} \tag{1}$$

where $[l_3 \quad 0 \quad m_3]^{\mathrm{T}}$ represents the unit vector along the direction of the second P joint, $[p_4 \quad 0 \quad q_4]^{\mathrm{T}}$ is the moment of the screw axis of the first R joint in the U joint with respect to the B-$x_by_bz_b$ frame, and $[l_5 \quad 0 \quad m_5]^{\mathrm{T}}$ and $[p_5 \quad q_5 \quad r_5]^{\mathrm{T}}$ are the unit vector and moment of the screw axis of the second R joint in the U joint described in the B-$x_by_bz_b$ frame, respectively. Here, $l_3, m_3, p_4, q_4, l_5, m_5, p_5, q_5$, and r_5 denote a certain constant of the unit vector, respectively.

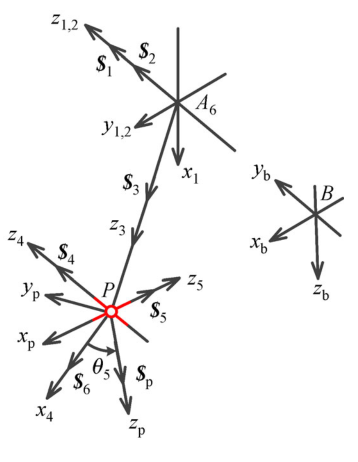

Fig. 3 Diagram of the twist system for the PRPU limb.

The wrench system of the PRPU branch chain is obtained by solving the reciprocal screw in Eq. (1) as follows:

$$\$^{\mathrm{r}} = [0 \quad 0 \quad 0; \quad m_5 \quad 0 \quad -l_5]^{\mathrm{T}}, \tag{2}$$

where $\$^{\mathrm{r}}$ denotes the constraint couple along the normal of the plane, the constraint couple is formed by the two revolute joints in the U joint. Here, the superscript r represents the abbreviation of reciprocal.

The constraint couple $\$^{\mathrm{r}}$ constrains the instantaneous twist $\$_6 = [m_5 \quad 0 \quad -l_5; \quad p_6 \quad q_6 \quad r_6]^{\mathrm{T}}$, which represents the rotational motion around the normal of the joint plane of the U joint. $\$_{\mathrm{p}}$ is assumed to be the twist of the moving platform's normal axis, and $\$_{\mathrm{p}}$ rotates θ_5 about $\$_5$. $\$_6$ intersects with $\$_{\mathrm{p}}$ and $\theta_5 \neq 90°$ in general. It shows the reciprocal product $\$^{\mathrm{r}} \circ \$_{\mathrm{p}} \neq 0$, which indicates that the virtual work of the constraint couple $\$^{\mathrm{r}}$ on the rotation about the moving platform's normal direction is not zero. It also implies that $\$^{\mathrm{r}}$ always constrains the moving platform's rotation about its normal line. Consequently, the 5PUS-PRPU parallel manipulator has five DOFs, three of which are translational and two are rotational (3T2R).

3.2 Inverse kinematics

Given that the reconfigurable base is fixed while the end-effector is moving, the main problem of inverse kinematics focuses on the 5PUS-PRPU parallel manipulator in this section. Then, the inverse problem is converted to solve the motion S_i of the P joint in the PUS limb when the moving platform's pose (x, y, z, α, and β) is know. Here, x, y, and z denote the displacement of the center of moving platform along x_b, y_b, and z_b axis respectively, and α and β are the rotation angle of the moving platform about x_b and y_b axis, respectively.

The pose transformation from P-$x_py_pz_p$ to B-$x_by_bz_b$ is obtained through the rotation of α about the x_b axis and the rotation of β about the y_p axis. Thus, matrix ${}^B\boldsymbol{R}_P$ can be presented as

$$\begin{aligned} {}^B\boldsymbol{R}_P &= \mathrm{rot}(x_b, \alpha)\mathrm{rot}(y_p, \beta) \\ &= \begin{bmatrix} \cos\beta & 0 & \sin\beta \\ \sin\alpha\sin\beta & \cos\alpha & -\sin\alpha\cos\beta \\ -\cos\alpha\sin\beta & \sin\alpha & \cos\alpha\cos\beta \end{bmatrix}. \end{aligned} \tag{3}$$

In reference to Fig. 4, we obtain

$$\boldsymbol{p}+\boldsymbol{r}_i=\boldsymbol{b}_i+s_i\boldsymbol{n}_i+l_i\boldsymbol{k}_i, \tag{4}$$

where $\boldsymbol{p}$ is point P's position vector relative to B-$x_\mathrm{b}y_\mathrm{b}z_\mathrm{b}$, $\boldsymbol{r}_i={}^B\boldsymbol{R}_P{}^\mathrm{p}\boldsymbol{r}_i$, and $\boldsymbol{r}_i$ and ${}^\mathrm{p}\boldsymbol{r}_i$ are the vector $\overrightarrow{PD_i}$ described in B-$x_\mathrm{b}y_\mathrm{b}z_\mathrm{b}$ and P-$x_\mathrm{p}y_\mathrm{p}z_\mathrm{p}$ frames, respectively. b_i is the vector $\overrightarrow{BA_i}$ represented in the B-$x_\mathrm{b}y_\mathrm{b}z_\mathrm{b}$ frame, and $\boldsymbol{n}_i$ and $\boldsymbol{k}_i$ denote the unit vectors of $\overrightarrow{A_iC_i}$ and $\overrightarrow{C_iD_i}$ described in the B-$x_\mathrm{b}y_\mathrm{b}z_\mathrm{b}$ frame, respectively. s_i denotes the motion of the driving joint P in the ith PUS branch chain, and l_i represents the length of C_iD_i.

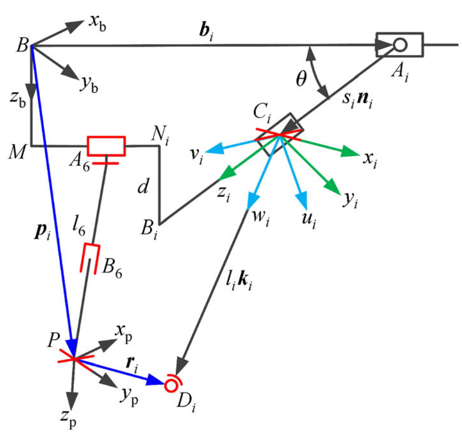

Fig. 4 Diagram of the ith PUS branch.

The vectors mentioned above are given as

$$\boldsymbol{p}_i=\begin{bmatrix}x\\y\\z\end{bmatrix},\ {}^\mathrm{p}\boldsymbol{r}_i=\begin{bmatrix}r_\mathrm{p}\cos\phi_i\\r_\mathrm{p}\sin\phi_i\\0\end{bmatrix},$$

$$\boldsymbol{b}_i=\begin{bmatrix}(L\cos\theta+r_\mathrm{m})\cos\varphi_i\\(L\cos\theta+r_\mathrm{m})\sin\varphi_i\\0\end{bmatrix},\ \boldsymbol{n}_i=\begin{bmatrix}-\cos\theta\cos\varphi_i\\-\cos\theta\sin\varphi_i\\\sin\theta\end{bmatrix}, \tag{5}$$

where L is limb A_iB_i's length and r_m and r_p denote the length of MN_i and PD_i, respectively. θ represents the acute angle between A_iB and A_iB_i.

By substituting Eqs. (3) and (5) into Eq. (4), Eq. (6) is obtained as

$$s_{\mathrm{a}i}s_i^2+s_{\mathrm{b}i}s_i+s_{\mathrm{c}i}=0, \tag{6}$$

where

$$\begin{cases}s_{\mathrm{a}i}=B_{xi}^2+B_{yi}^2+B_{zi}^2,\\s_{\mathrm{b}i}=2(A_{xi}B_{xi}+A_{yi}B_{yi}+A_{zi}B_{zi}),\\s_{\mathrm{c}i}=A_{xi}^2+A_{yi}^2+A_{zi}^2-l_i^2,\end{cases}$$

where

$$\begin{cases}A_{xi}=x+r_\mathrm{p}\cos\phi_i\cos\beta+r_\mathrm{p}\sin\phi_i\sin\beta\sin\alpha\\\qquad-(L\cos\theta+r_\mathrm{m})\cos\varphi_i,\\B_{xi}=\cos\theta\cos\varphi_i,\\A_{yi}=y+r_\mathrm{p}\sin\phi_i\cos\alpha-(L\cos\theta+r_\mathrm{m})\sin\varphi_i,\\B_{yi}=\cos\theta\sin\varphi_i,\\A_{zi}=z+r_\mathrm{p}\sin\phi_i\cos\beta\sin\alpha-r_\mathrm{p}\cos\phi_i\sin\beta,\\B_{zi}=-\sin\theta.\end{cases}$$

Equation (6) yields

$$s_i=\frac{-s_{\mathrm{b}i}\pm\sqrt{s_{\mathrm{b}i}^2-4s_{\mathrm{a}i}s_{\mathrm{c}i}}}{2s_{\mathrm{a}i}}. \tag{7}$$

The determination of the symbol of s_i depends on the structural features of the proposed HPM. According to the kinematics simulation of the manipulator in Ref. [16], the negative symbol of s_i should be selected as the inverse solution of the manipulator.

3.3 Rotation angles of the U joint in the PUS limb

Local coordinate systems should be established for a convenient kinematics analysis. As shown in Fig. 4, the local coordinate system C_i-$x_iy_iz_i$ for the ith PUS branch is built at C_i, and the x_i axis is along the U joint's inner rotational axis. The z_i axis is along the direction of the straight line A_iB_i. The system C_i-$u_iv_iw_i$ is established at the point C_i to facilitate the representation of the pose of the PUS limbs. The w_i axis is along the direction of the vector $\overrightarrow{C_iD_i}$, and the v_i axis is coincident with the U joint's outer rotational axis. Here, y_i and u_i axes conform to the right-hand rule.

Then, the pose transformation of C_i-$u_iv_iw_i$ relative to the system C_i-$x_iy_iz_i$ can be achieved by two continuous rotations of γ_i and η_i about the x_i and v_i axes, respectively. Thus, transformation matrix $\boldsymbol{R}_{0i}$ is expressed as

$$\boldsymbol{R}_{0i}=\mathrm{rot}(x_i,\ \gamma_i)\mathrm{rot}(v_i,\ \eta_i)$$
$$=\begin{bmatrix}\cos\eta_i&0&\sin\eta_i\\\sin\gamma_i\sin\eta_i&\cos\gamma_i&-\cos\eta_i\sin\gamma_i\\-\cos\gamma_i\sin\eta_i&\sin\gamma_i&\cos\gamma_i\cos\eta_i\end{bmatrix}. \tag{8}$$

Similarly, transformation from system C_i-$x_iy_iz_i$ to system B-$x_\mathrm{b}y_\mathrm{b}z_\mathrm{b}$ can be achieved by two continuous rotations of angles φ_i and θ about the z_b axis and the new y_b axis. Rotation matrix ${}^B\boldsymbol{R}_i$ is given as

$$
{}^{B}\boldsymbol{R}_i = \mathrm{rot}(z_\mathrm{b},\ \varphi_i)\mathrm{rot}\left(y_\mathrm{b},\ -\left(\frac{\pi}{2}-\theta\right)\right)\mathrm{rot}\left(z_\mathrm{b},\ \frac{\pi}{2}\right)
$$

$$
= \begin{bmatrix} -\sin\varphi_i & -\cos\varphi_i\sin\theta & -\cos\theta\cos\varphi_i \\ \cos\varphi_i & -\sin\theta\sin\varphi_i & -\cos\theta\sin\varphi_i \\ 0 & -\cos\theta & \sin\theta \end{bmatrix}. \tag{9}
$$

On the basis of the two transformation matrices, the transformation matrix from C_i-$u_iv_iw_i$ to B-$x_\mathrm{b}y_\mathrm{b}z_\mathrm{b}$ can be given as

$$
{}^{B}\boldsymbol{R}_{0i} = {}^{B}\boldsymbol{R}_i\boldsymbol{R}_{0i} = \begin{bmatrix} u_{ix} & v_{ix} & w_{ix} \\ u_{iy} & v_{iy} & w_{iy} \\ u_{iz} & v_{iz} & w_{iz} \end{bmatrix}
$$

$$
= [\boldsymbol{u}_i \quad \boldsymbol{v}_i \quad \boldsymbol{w}_i],\ i = 1,\ 2,\ \ldots,\ 5, \tag{10}
$$

where

$$
\begin{cases}
u_{ix} = \cos(\gamma_i+\theta)\cos\varphi_i\sin\eta - \cos\eta_i\sin\varphi_i, \\
u_{iy} = \cos\eta_i\cos\varphi_i + \cos(\gamma_i+\theta)\sin\eta_i\sin\varphi_i, \\
u_{iz} = -\sin\eta_i\sin(\gamma_i+\theta), \\
v_{ix} = -\cos\varphi_i\sin(\gamma_i+\theta), \\
v_{iy} = -\sin(\gamma_i+\theta)\sin\varphi_i, \\
v_{iz} = -\cos(\gamma_i+\theta), \\
w_{ix} = -\cos\eta_i\cos(\gamma_i+\theta)\cos\varphi_i - \sin\eta_i\sin\varphi_i, \\
w_{iy} = \cos\varphi_i\sin\eta_i - \cos\eta_i\cos(\gamma_i+\theta)\sin\varphi_i, \\
w_{iz} = \cos\eta_i\sin(\gamma_i+\theta),
\end{cases}
$$

where vectors $\boldsymbol{u}_i$, $\boldsymbol{v}_i$, and $\boldsymbol{w}_i$ are the unit vectors of u_i, v_i, and w_i axes in system B-$x_\mathrm{b}y_\mathrm{b}z_\mathrm{b}$, respectively.

Thus, angles γ_i and η_i can be derived as follows:

$$
\begin{cases}
\gamma_i = \arctan\dfrac{-w_{iz}}{w_{ix}\cos\varphi_i + w_{iy}\sin\varphi_i} - \theta, \\
\eta_i = -\arcsin(w_{iy}\cos\varphi_i - w_{ix}\sin\varphi_i),
\end{cases} \tag{11}
$$

where γ_i and η_i represent the rotational angles of the two perpendicular axes of the U joint.

4 Jacobian matrix

The Jacobian matrix of HPM is formulated in accordance with screw theory [37]. The screws of each joint are illustrated in Fig. 5.

By combining the instantaneous twists of all the PUS limbs, the infinitesimal twist of the end-effector is obtained as

$$
\$_P = \dot{s}_i\$_{1,i} + \sum_{j=2}^{6}\delta\mu_{j,i}\$_{j,i},\ i = 1, 2, \ldots, 5, \tag{12}
$$

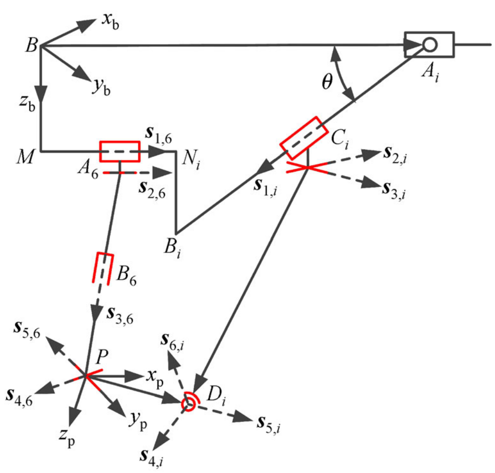

Fig. 5 Screws of the ith PUS and the middle branch chains.

where $\$_P$ is the infinitesimal twist of the perfusion platform, $\$_{1,i}$ and $\$_{j,i}$ represent the unit screw of the first P and the jth 1-DOF joint for the ith PUS branch chain, respectively, s_i denotes the velocity of the ith driving joint P, $\delta\mu_{j,i}$ denotes the angular velocity in response to the unit screw $\$_{j,i}$ of the ith limb, and

$$
\$_{1,i} = \begin{bmatrix} \boldsymbol{0}_{3\times1} \\ \boldsymbol{s}_{1,i} \end{bmatrix},\ \$_{2,i} = \begin{bmatrix} \boldsymbol{s}_{2,i} \\ (\boldsymbol{r}_i - l_i\boldsymbol{k}_i)\times\boldsymbol{s}_{2,i} \end{bmatrix},
$$

$$
\$_{3,i} = \begin{bmatrix} \boldsymbol{s}_{3,i} \\ (\boldsymbol{r}_i - l_i\boldsymbol{k}_i)\times\boldsymbol{s}_{3,i} \end{bmatrix},\ \$_{4,i} = \begin{bmatrix} \boldsymbol{s}_{4,i} \\ \boldsymbol{r}_i\times\boldsymbol{s}_{4,i} \end{bmatrix},
$$

$$
\$_{5,i} = \begin{bmatrix} \boldsymbol{s}_{5,i} \\ \boldsymbol{r}_i\times\boldsymbol{s}_{5,i} \end{bmatrix},\ \$_{6,i} = \begin{bmatrix} \boldsymbol{s}_{6,i} \\ \boldsymbol{r}_i\times\boldsymbol{s}_{6,i} \end{bmatrix}.
$$

This work assumes that the driving joints of all the PUS limbs are locked. Then, the reciprocal screw $\hat{\$}^{\mathrm{r}}_{1,i}$ for the ith PUS limb is expressed as

$$
\hat{\$}^{\mathrm{r}}_{1,i} = \begin{bmatrix} \boldsymbol{k}_i \\ \boldsymbol{r}_i\times\boldsymbol{k}_i \end{bmatrix}. \tag{13}
$$

Given that $\hat{\$}^{\mathrm{r}}_{1,i}\circ\$_{j,i} = 0$ and $\boldsymbol{s}_{1,i} = \boldsymbol{n}_i$, multiplying with $\hat{\$}^{\mathrm{r}}_{1,i}$ on both sides of Eq. (12) produces

$$
\hat{\$}^{r}_{1,i}\circ\$_P = \dot{s}_i\boldsymbol{k}_i^{\mathrm{T}}\boldsymbol{n}_i,\ i = 1,\ 2,\ \ldots,\ 5. \tag{14}
$$

Recasting Eq. (14) into a matrix form results in

$$
\boldsymbol{J}_P\$_P = \boldsymbol{J}_\mathrm{d}\dot{\boldsymbol{s}}_\mathrm{d}, \tag{15}
$$

where $\dot{\boldsymbol{s}}_\mathrm{d}$ denote the velocity vector of the five driving joints of the PUS limb, and $\boldsymbol{J}_P$ and $\boldsymbol{J}_\mathrm{d}$ are the coefficient of $\$_P$ and $\dot{\boldsymbol{s}}_\mathrm{d}$, respectively.

$$\begin{cases} \dot{\boldsymbol{s}}_{\mathrm{d}} = [\dot{s}_1 \quad \dot{s}_2 \quad \dot{s}_3 \quad \dot{s}_4 \quad \dot{s}_5]^{\mathrm{T}}, \\ \boldsymbol{J}_{\mathrm{d}} = \mathrm{diag}(\boldsymbol{k}_1^{\mathrm{T}}\boldsymbol{n}_1 \quad \boldsymbol{k}_2^{\mathrm{T}}\boldsymbol{n}_2 \quad \boldsymbol{k}_3^{\mathrm{T}}\boldsymbol{n}_3 \quad \boldsymbol{k}_4^{\mathrm{T}}\boldsymbol{n}_4 \quad \boldsymbol{k}_5^{\mathrm{T}}\boldsymbol{n}_5) \in \mathbb{R}^{5\times 5}, \\ \boldsymbol{J}_P = \begin{bmatrix} \boldsymbol{k}_1 & \boldsymbol{k}_2 & \boldsymbol{k}_3 & \boldsymbol{k}_4 & \boldsymbol{k}_5 \\ \boldsymbol{r}_1\times\boldsymbol{k}_1 & \boldsymbol{r}_2\times\boldsymbol{k}_2 & \boldsymbol{r}_3\times\boldsymbol{k}_3 & \boldsymbol{r}_4\times\boldsymbol{k}_4 & \boldsymbol{r}_5\times\boldsymbol{k}_5 \end{bmatrix}^{\mathrm{T}} \in \mathbb{R}^{5\times 6}. \end{cases}$$

The end-effector's infinitesimal twist can be obtained by combining the instantaneous twists of the passive PRPU limb. Then, we obtain

$$\boldsymbol{\$}_P = \sum_{j=1}^{5} \delta\mu_{j,6}\boldsymbol{\$}_{j,6}, \tag{16}$$

where $\delta\mu_{j,6}$ and $\boldsymbol{\$}_{j,6}$ have the same physical meaning as $\delta\mu_{j,i}$ and $\boldsymbol{\$}_{j,i}$, and

$$\boldsymbol{\$}_{1,6} = \begin{bmatrix} \boldsymbol{0}_{3\times 1} \\ \boldsymbol{s}_{1,6} \end{bmatrix},\ \boldsymbol{\$}_{2,6} = \begin{bmatrix} \boldsymbol{s}_{2,6} \\ -l_6\boldsymbol{k}_6\times\boldsymbol{s}_{2,6} \end{bmatrix},\ \boldsymbol{\$}_{3,6} = \begin{bmatrix} \boldsymbol{0}_{3\times 1} \\ \boldsymbol{k}_6 \end{bmatrix},$$

$$\boldsymbol{\$}_{4,6} = \begin{bmatrix} \boldsymbol{s}_{4,6} \\ \boldsymbol{0}_{3\times 1} \end{bmatrix},\ \boldsymbol{\$}_{5,6} = \begin{bmatrix} \boldsymbol{s}_{5,6} \\ \boldsymbol{0}_{3\times 1} \end{bmatrix}, \tag{17}$$

where l_6 denotes the distance from point A_6 to point P.

Multiplying with $\hat{\boldsymbol{\$}}^{\mathrm{r}}_{j,6}$ on both sides of Eq. (16) yields

$$\hat{\boldsymbol{\$}}^{\mathrm{r}}_{j,6} \circ \boldsymbol{\$}_P = 0, \tag{18}$$

where $\hat{\boldsymbol{\$}}^{\mathrm{r}}_{j,6} = \begin{bmatrix} \boldsymbol{0}_{3\times 1} \\ \boldsymbol{n}_{45} \end{bmatrix}$, $\boldsymbol{n}_{45} = \boldsymbol{s}_{4,6}\times\boldsymbol{s}_{5,6}$.

Combining Eqs. (14) and (18) leads to

$$\dot{\boldsymbol{s}} = \boldsymbol{J}_1\boldsymbol{J}_2\boldsymbol{\$}_P = \boldsymbol{J}\boldsymbol{\$}_P, \tag{19}$$

where $\boldsymbol{J} = \boldsymbol{J}_1\boldsymbol{J}_2$ is the 5PUS-PRPU parallel manipulator's entire Jacobian matrix, and

$$\dot{\boldsymbol{s}} = [\dot{s}_1 \quad \dot{s}_2 \quad \dot{s}_3 \quad \dot{s}_4 \quad \dot{s}_5 \quad 0]^{\mathrm{T}},\ \boldsymbol{J}_1 = \begin{bmatrix} \boldsymbol{J}_{\mathrm{a}}^{-1} & \boldsymbol{0} \\ \boldsymbol{0} & 0 \end{bmatrix},$$

$$\boldsymbol{J}_2 = \begin{bmatrix} \boldsymbol{k}_1 & \boldsymbol{k}_2 & \boldsymbol{k}_3 & \boldsymbol{k}_4 & \boldsymbol{k}_5 & \boldsymbol{0}_{1\times 3} \\ \boldsymbol{r}_1\times\boldsymbol{k}_1 & \boldsymbol{r}_2\times\boldsymbol{k}_2 & \boldsymbol{r}_3\times\boldsymbol{k}_3 & \boldsymbol{r}_4\times\boldsymbol{k}_4 & \boldsymbol{r}_5\times\boldsymbol{k}_5 & \boldsymbol{n}_{45} \end{bmatrix}^{\mathrm{T}},$$

$$\boldsymbol{\$}_P = \begin{bmatrix} \dot{x} & \dot{y} & \dot{z} & \dot{\alpha} & \dot{\beta} & 0 \end{bmatrix}^{\mathrm{T}}.$$

Equation (19) indicates that the last row of the Jacobian matrix $\boldsymbol{J}$ is zero. Furthermore, the element of the last row of the vector $\boldsymbol{\$}_P$ is zero. Therefore, Eq. (19) describing the relationship between vector $\boldsymbol{\$}_P$ and vector $\dot{\boldsymbol{s}}$ can be rewritten as

$$\dot{\boldsymbol{s}}_{\mathrm{d}} = \boldsymbol{J}_{\mathrm{d}}^{-1}\boldsymbol{J}'_P\boldsymbol{\$}'_P = \boldsymbol{J}'\boldsymbol{\$}'_P, \tag{20}$$

where $\boldsymbol{J}' = \boldsymbol{J}_{\mathrm{d}}^{-1}\boldsymbol{J}'_P$, $\boldsymbol{J}'_P \in \mathbb{R}^{5\times 5}$ is the first five columns of the matrix $\boldsymbol{J}_P$ and $\boldsymbol{\$}'_P = \begin{bmatrix} \dot{x} & \dot{y} & \dot{z} & \dot{\alpha} & \dot{\beta} \end{bmatrix}^{\mathrm{T}}$.

The problem where the Jacobian matrix has inconsistent dimensions arises because the proposed HPM has three translational and two rotational DOFs, and this problem leads to an unclear physical meaning of the condition number of Eq. (20). Therefore, the Jacobian matrix must be normalized. In this section, the Jacobian matrix is normalized using the characteristic length. Then, the column vectors of the Jacobian matrix that are grouped based on dimension can be obtained as

$$\boldsymbol{J}' = [\boldsymbol{J}'(:,1:3) \quad \boldsymbol{J}'(:,4:5)]. \tag{21}$$

Characteristic length D [38] is defined as

$$D = \sqrt{\frac{m_1\mathrm{tr}[\boldsymbol{J}'(:,4:5)^{\mathrm{T}}\boldsymbol{J}'(:,4:5)]}{m_2\mathrm{tr}[\boldsymbol{J}'(:,1:3)^{\mathrm{T}}\boldsymbol{J}'(:,1:3)]}}, \tag{22}$$

where m_1 and m_2 represent the number of translational and rotational DOFs, respectively, and $m_1 = 3$ and $m_2 = 2$. tr[] is the sum of the main diagonal elements of the matrix.

The dimensionally consistent Jacobian matrix is then expressed as

$$\boldsymbol{J}'_{\mathrm{c}} = \left[\boldsymbol{J}'(:,1:3) \quad \frac{1}{D}\boldsymbol{J}'(:,4:5)\right]. \tag{23}$$

5 Dimensional synthesis

In this section, an analysis of the dimensional synthesis of HPM subject to several related constraints is conducted. The goal of the research on dimensional synthesis can be explained as the determination of the kinematic parameters that can achieve excellent kinematic performance in the task workspace. The work in this section mainly involves the establishment of design variables, constraints, performance indices, and objective function and optimization of the design.

5.1 Design variables

As described in Ref. [16], task workspace T_w is represented by the minimum cuboid that can cover the task honeycombs. In the following sections, the evaluation of performance indices is conducted in this prescribed workspace. Figure 6 shows the extreme position of HPM in T_w. H is the perpendicular distance measured from point B to point P, and R and h are the radius and height of T_w. We let L, l, r_p, H, and h be normalized by r_m (as shown in Fig. 6). The variables can be obtained as follows:

$$\lambda_1 = \frac{L}{r_m},\ \lambda_2 = \frac{l}{r_m},\ \lambda_3 = \frac{r_p}{r_m},\ \lambda_4 = \frac{H}{r_m},\ \lambda_5 = \frac{h}{R}, \tag{24}$$

where λ_5 represents the height/radius ratio of T_w. For the proposed HPM, the value of λ_5 should be constant.

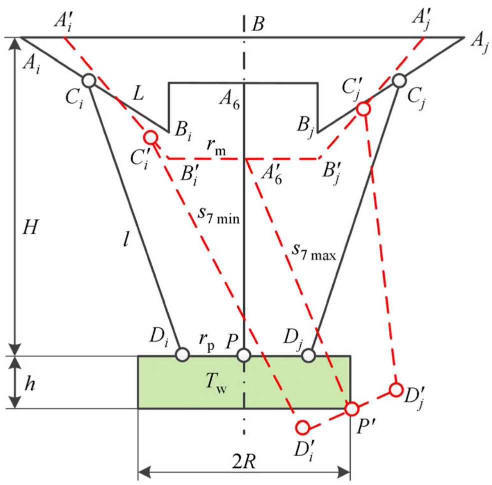

Fig. 6 Pose of HPM in the task workspace.

The dimensional synthesis is explained as follows: Under the condition of known λ_5 and several mechanical constraints, the optimal values of λ_1, λ_2, λ_3, and λ_4 are determined so that good kinematic performance can be obtained in T_w.

On the basis of the task workspace and variables shown above, the extreme lengths of the PRPU limb can be easily presented as

$$\begin{cases} s_{7\min} = H - L\sin\theta + d = r_m(\lambda_4 - \lambda_1 \sin\theta) + d, \\ s_{7\max} = \sqrt{R^2 + (H + h - L\sin\theta + d)^2} \\ \quad\quad = \sqrt{R^2 + [r_m(\lambda_4 - \lambda_1 \sin\theta) + d + h]^2}, \end{cases} \tag{25}$$

where $s_{7\min}$ and $s_{7\max}$ are the minimum and maximum displacements of the second P joint in the PRPU branch chain and d is the length of N_iB_i.

Similarly, the driving joints' displacements in the PUS branch chains, including $s_{i\min}$ and $s_{i\max}$ $(i = 1, 2, ..., 5)$, can be obtained in accordance with the inverse kinematics and the proposed design variables.

5.2 Performance indices

In research on the parallel manipulator's kinematic performance, the condition number κ of the Jacobian matrix is usually used to evaluate local kinematic performance. However, the value of κ varies with the different structural configurations of the manipulator. Thus, a global performance index related to the condition number needs to be introduced. In reference to the performance indices presented in Ref. [33], two performance indices are obtained as follows:

$$\bar{\kappa} = \frac{\int_V \kappa \mathrm{d}V}{V}, \tag{26}$$

$$\tilde{\kappa} = \frac{\sqrt{\int_V (\kappa - \bar{\kappa})^2 \mathrm{d}V}}{V}, \tag{27}$$

where $\kappa = \sigma_{\max}/\sigma_{\min}$, $\sigma_{\max}$ and $\sigma_{\min}$ denote the maximal and minimal eigenvalues of Jacobian matrix J, respectively, $\bar{\kappa}$ represents the mean value of κ in T_w, V represents the volume of T_w, and $\tilde{\kappa}$ is the standard deviation of κ relative to $\bar{\kappa}$ in T_w.

5.3 Design constraints

Based on the considerations of the practical perfusion of the proposed HPM, several structure constraints are given in detail for the dimensional synthesis analysis. Here, given $\lambda_5 = 0.5$, we investigate the effects of variables λ_1, λ_2, λ_3, and λ_4 on the established kinematic performance indices. Figure 7(a) shows the comparison of condition number κ with different x and y when λ_1 is equal to 1.5, 1.9, and 2.3. In this case, the values for λ_2, λ_3, and λ_4 are constant, and α, β, z, θ, and r_m are equal to $-30°$, $-10°$, 1200 mm, 30°, and 700 mm, respectively.

Similarly, comparisons of κ when λ_2 and λ_3 have different values are displayed in Figs. 7(b) and 7(c), respectively. When λ_2 or λ_3 is the variable, all of the other parameters are constants. Figures 7(d) to 7(f) show comparisons of the orientation workspace of the moving platform with the change in α and β when λ_1, λ_2, and λ_3 have different values, respectively. In this case, x, y, z, θ, and r_m are equal to 0, 0, 1200 mm, 30°, and 700 mm, respectively. The comparisons in Fig. 7 reveal that large λ_1 and λ_2 help improve the kinematic performance and increase the orientation workspace. The comparisons also imply that the achievement of good kinematic performance comes at the cost of increasing the volume of the hybrid mechanism. Thus, the final values of λ_1 and λ_2 should be determined properly. Meanwhile, a small λ_3 improves the

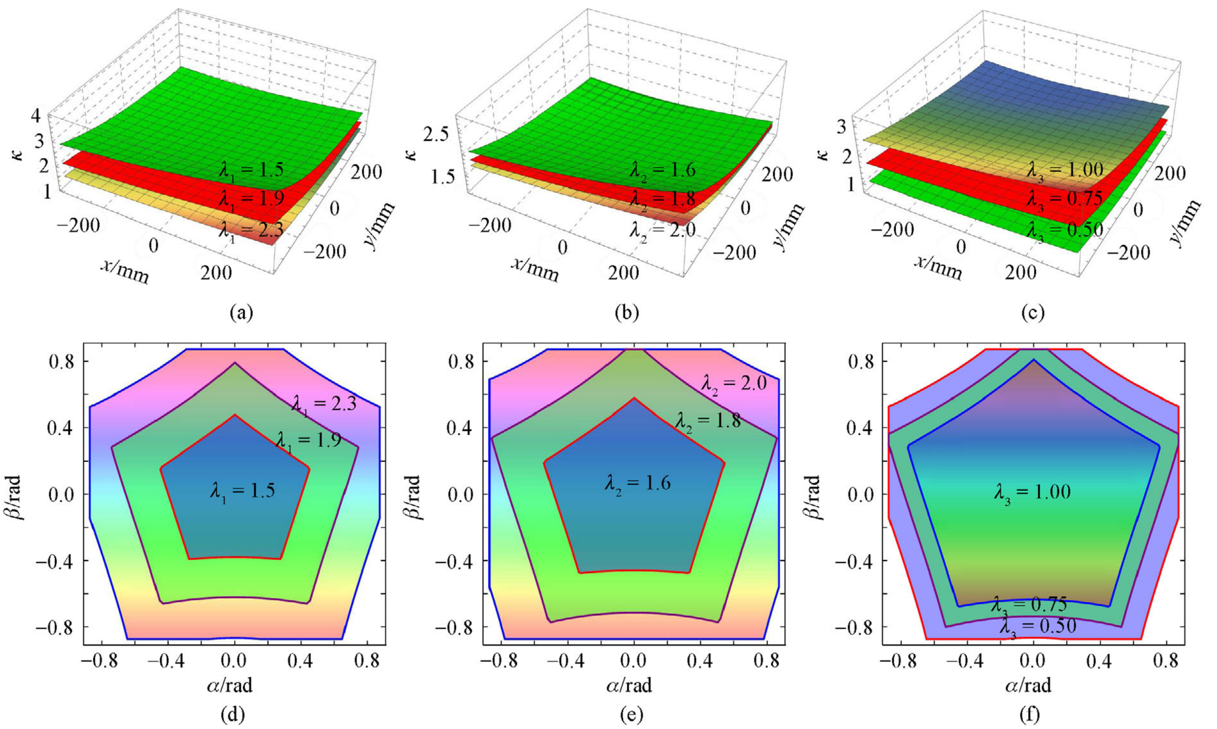

Fig. 7 Comparisons of condition numbers and orientation workspace with different λ_1, λ_2, and λ_3 values: Condition number with (a) different λ_1, (b) different λ_2, and (c) different λ_3; orientation workspace with (d) different λ_1, (e) different λ_2, and (f) different λ_3.

orientation workspace of the proposed HPM.

In consideration of the requirements of installing the perfusion device on the moving platform, the values of λ_1 and λ_2 should be smaller than a certain value. Moreover, the value of r_p should be smaller than r_m to avoid direct kinematic singularity. Thus, the constraints for λ_1, λ_2, and λ_3 can be expressed as

$$\begin{cases} \lambda_1 \leqslant \lambda_{1\max}, \\ \lambda_2 \leqslant \lambda_{2\max}, \\ \lambda_{3\min} \leqslant \lambda_3 \leqslant 1, \end{cases} \tag{28}$$

where $\lambda_{1\max}$ and $\lambda_{2\max}$ represent the maximum values of λ_1 and λ_2, respectively, and $\lambda_{3\min}$ is the minimum value of λ_3 in the mechanism design.

For the PUS limb, the displacement s_i of the driving slider should be within the region of the link A_iB_i. Then, the constraint is given as

$$0 \leqslant s_i \leqslant L. \tag{29}$$

The ratio of the stroke of the PRPU middle limb should be as small as possible to guarantee the stiffness of the middle passive limb. In addition, the range of movement for the first P joint of the passive limb is constrained by the size of the middle platform. Therefore, the two constraints can be obtained as

$$\begin{cases} -r_m < s_6 < r_m, \\ \chi = \dfrac{s_{7\max} - s_{7\min}}{s_{7\min}} \leqslant \chi_{\max}, \end{cases} \tag{30}$$

where s_6 is the motion of the first P joint in the PRPU branch chain and $\chi_{\max}$ denotes the maximum allowable value of χ. In consideration of the requirements for the workspace and stiffness of HPM, $\chi_{\max}$ is between 0.7 and 0.8.

Apart from the above-mentioned constraints, the angle range of the U joint for the PUS limb should also be considered to avoid the interference between kinematic branch chains. As shown in Fig. 8, the variations of the rotation angles γ_i and η_i of the U joint versus α and β are given when x, y, z, θ, and r_m have values of 350 mm, 350 mm, 1100 mm, 30°, and 600 mm, respectively. According to these figures, the maximum angles of γ_i and η_i are 40.915° and 43.599°. Consequently, the angles of γ_i and η_i need to be constrained, and the constraint equations can be expressed as

$$\begin{cases} |\gamma_i| \leqslant \gamma_{\max}, \\ |\eta_i| \leqslant \eta_{\max}, \end{cases} \tag{31}$$

where $\gamma_{\max}$ and $\eta_{\max}$ are the maximum allowable values of γ_i and η_i, respectively.

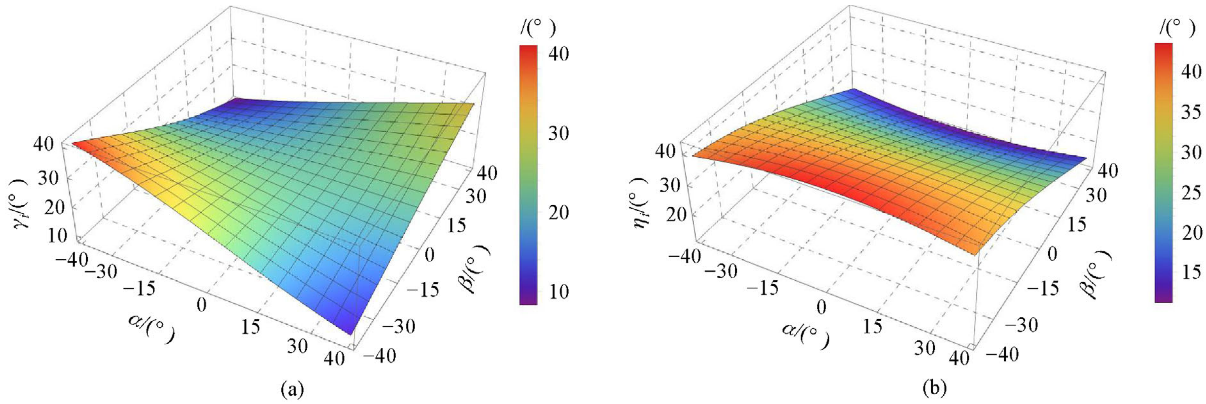

Fig. 8 (a) γ_i and (b) η_i with the change in α and β.

5.4 Objective function

Figures 9(a) and 9(b) show the variations of $\bar{\kappa}$ and $\tilde{\kappa}$ versus λ_1, λ_2, and λ_4, in the task workspace when λ_3, α, β, and θ have constant values. The curves of $\bar{\kappa}$ indicate that the overall value of $\bar{\kappa}$ increases with the increase in λ_4 regardless of the values of λ_1 and λ_2. Moreover, a large λ_1 and a small λ_2 help enhance the kinematic performance of HPM. However, the variations of $\tilde{\kappa}$ with the change in λ_4 exhibit a different trend compared with the variation of $\tilde{\kappa}$. The variations of $\bar{\kappa}$ and $\tilde{\kappa}$ in terms of λ_1, λ_3, and λ_4 also change in an opposite trend when λ_2 and θ are given, as

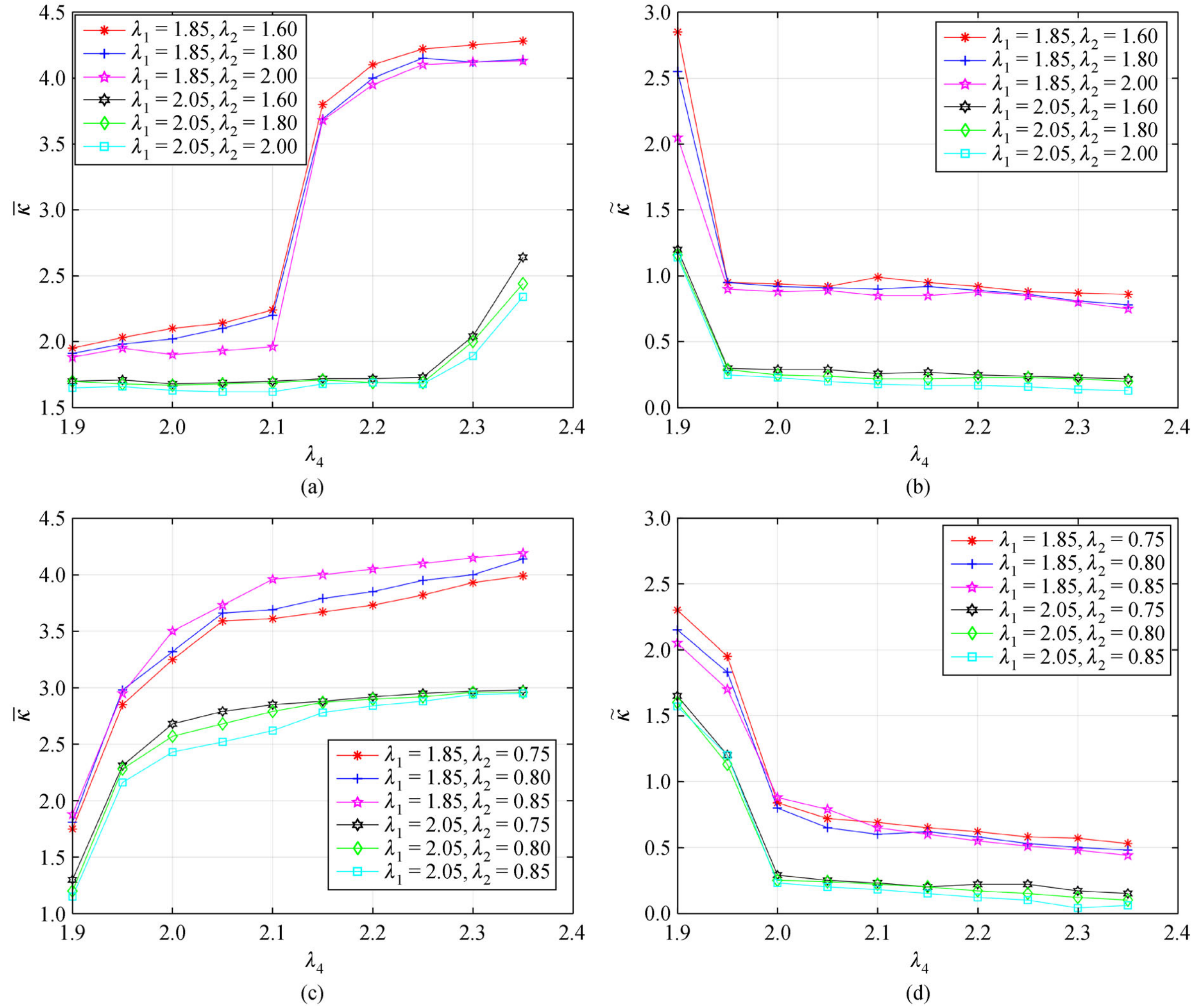

Fig. 9 (a) $\bar{\kappa}$ and (b) $\tilde{\kappa}$ with the change in λ_1, λ_2, and λ_4; (c) $\bar{\kappa}$ and (d) $\tilde{\kappa}$ with the change in λ_1, λ_3, and λ_4.

shown in Figs. 9(c) and 9(d). Consequently, a global and comprehensive objective function ε is proposed to obtain the variable values that are optimal for $\bar{\kappa}$ and $\tilde{\kappa}$ [33].

$$\varepsilon = \sqrt{\bar{\kappa}^2 + (\rho_\varepsilon \tilde{\kappa})^2}, \tag{32}$$

where ρ_ε represents the weight coefficient of $\tilde{\kappa}$.

5.5 Optimal design

In accordance with the structural features of the proposed HPM, the displacement of the end-effector along the z_b axis varies with different θ values. Specifically, for different values of θ, different optimization ranges should be adopted for λ_4. The optimization should be conducted under the condition that θ equals to a certain value. The optimization design of the proposed HPM concerning λ_1, λ_2, λ_3, and λ_4 is expressed as the following constrained nonlinear function:

$$\underset{\lambda_1,\lambda_2,\lambda_3,\lambda_4 \in \mathbb{R}}{\varepsilon(\lambda_1,\lambda_2,\lambda_3,\lambda_4,\theta) \to \min}, \tag{33}$$

which is subject to the constraints Eqs. (28)–(31).

5.6 Simulation examples

With the objective function proposed in Section 5.5, the optimal design for the HPM obtained with GA is developed in this section. On the basis of the task honeycombs described in Ref. [16], task workspace T_w can be expressed as

$$\begin{cases} -350\ \text{mm} \leqslant x \leqslant 350\ \text{mm}, \\ -350\ \text{mm} \leqslant y \leqslant 350\ \text{mm}, \\ H \leqslant z \leqslant H + h, \\ -35° \leqslant \alpha \leqslant 35°, \\ -35° \leqslant \beta \leqslant 35°. \end{cases} \tag{34}$$

In this work, $h = 210$ mm, $R = 350$ mm, $\lambda_5 = 0.6$, $z_{\min} = H$, and $z_{\max} = H + h$. We select $\rho_\varepsilon = 3$ for weighing the importance of $\tilde{\kappa}$. The other variables are given as $r_m = 700$ mm, $d = 310$ mm, $\gamma_{\max} = 45°$, and $\eta_{\max} = 45°$. For the proposed HPM, the smaller the value of θ is, the better the stiffness of the HPM is. Therefore, the maximum value of θ that can meet the perfusion of the boundary honeycombs is assumed to be 60°. Here, the values of θ are 20°, 30°, 40°, 50°, and 60°. The ranges for λ_1, λ_2, λ_3, and λ_4 with different values of θ are given in Table 1.

In accordance with the constraint equations and the ranges of the design variables, the objective function can be solved so that its minimal value can be obtained by MATLAB. The optimization results, including the fitness value of the objective function and current best individual values of the variables with different values of θ, are shown in Fig. 10. The best values for λ_1, λ_2, λ_3, and λ_4 when θ has different values are given in Table 2. The optimal value of objective function ε gradually increases with the increase in θ.

Table 1 Variable ranges of λ_1, λ_2, λ_3, and λ_4 with different θ values

θ/(°)	λ_1	λ_2	λ_3	λ_4
20	[1.8, 2.2]	[1.7, 2.1]	[0.6, 1.0]	[1.6, 1.9]
30	[1.8, 2.2]	[1.7, 2.1]	[0.6, 1.0]	[1.9, 2.2]
40	[1.8, 2.2]	[1.7, 2.1]	[0.6, 1.0]	[2.2, 2.5]
50	[1.8, 2.2]	[1.7, 2.1]	[0.6, 1.0]	[2.5, 2.8]
60	[1.8, 2.2]	[1.7, 2.1]	[0.6, 1.0]	[2.8, 3.1]

Table 2 shows five sets of values for λ_1, λ_2, λ_3, and λ_4. The analysis and verification of the workspace indicate that the orientation workspace of the end-effector with the first, second, third, and fourth sets of values of λ_1, λ_2, λ_3, and λ_4 cannot meet the perfusion of the boundary honeycombs. However, the last set of values can meet all of the honeycombs' perfusion on the spherical crown surface and is thus selected as the optimal values of the structural parameters of the proposed HPM. The workspace analysis for HPM in Ref. [16] indicates that the reachable workspace of the end-effector decreases gradually with the increase in the end-effector's displacement along the z_b axis. Thus, if the end-effector's reachable workspace can satisfy the task workspace when θ is 60°, then it can definitely satisfy the conditions when θ has values of 20°, 30°, 40°, and 50°. This condition proves that the selection method for the values of λ_1, λ_2, λ_3, and λ_4 mentioned above is reasonable. Based on the determined values of λ_1, λ_2, λ_3, and λ_4, the other parameters (including $s_{i\min}$, $s_{i\max}$, $s_{7\min}$, $s_{7\max}$, $z_{\min}$, and $z_{\max}$) with different values of θ are also computed, and they are shown in Table 3.

The optimization results in Table 3 indicate that the moving platform of the manipulator can achieve movement along the z_b axis from 1120 to 2170 mm, which meets the perfusion requirement of the position workspace. During the perfusion of all the honeycombs, the minimum and maximum displacements for the PUS limb are 47.81 and 1402.62 mm, respectively, which conform to the constraint in Eq. (29). The extreme lengths of the passive PRPU link are 915.00 and 1273.31 mm. Then, we obtain $\chi = 0.39$, which is in agreement with the constraint in Eq. (30). Thus, with the parameters in Table 3, the structure parameters of the proposed 5-DOF HPM are determined and shown as followings: $L = 1480$ mm, $l = 1420$ mm, $r_m = 700$ mm, $r_p = 490$ mm, $s_{i\min} = 47.81$ mm, $s_{i\max} = 1402.62$ mm, $s_{7\min} = 915.00$ mm, $s_{7\max} = 1273.31$ mm, $z_{\min} = 1120$ mm, $z_{\max} = 2170$ mm, $|\gamma_i|_{\max} = 18.15°$, $|\eta_i|_{\max} = 37.69°$. $|\gamma_i|_{\max}$ and $|\eta_i|_{\max}$ represent the maximum rotation values of the U joint in the PUS limb, which also meet the constraint in Eq. (31).

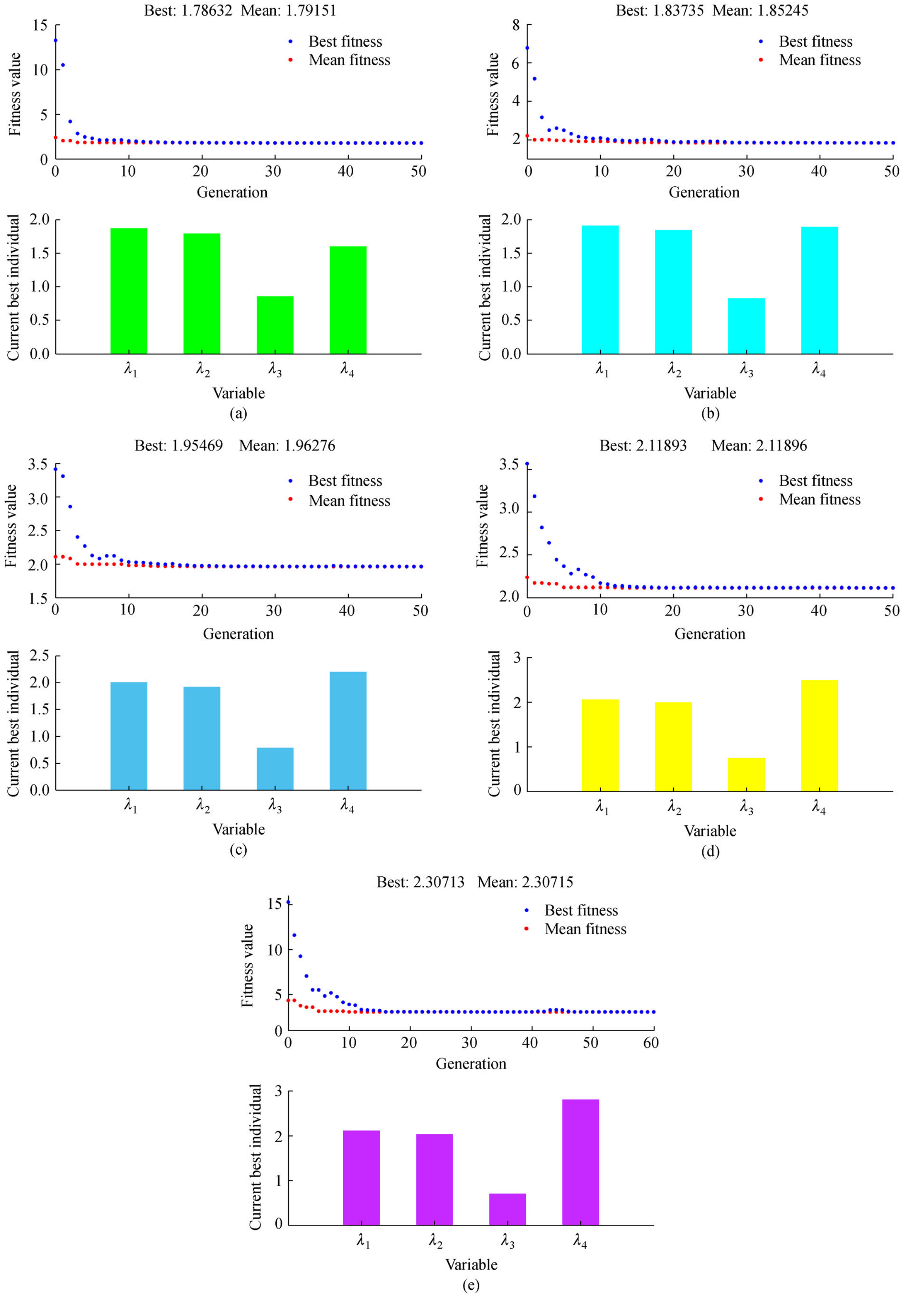

Fig. 10 Optimization results of λ_1, λ_2, λ_3, and λ_4 based on GA when (a) $\theta = 20°$, (b) $\theta = 30°$, (c) $\theta = 40°$, (d) $\theta = 50°$, and (e) $\theta = 60°$.

Table 2 Optimal values of λ_1, λ_2, λ_3, and λ_4 with different θ values

θ/(°)	λ_1	λ_2	λ_3	λ_4	ε_{min}
20	1.876	1.793	0.853	1.6	1.786
30	1.915	1.847	0.827	1.9	1.837
40	1.998	1.921	0.786	2.2	1.955
50	2.064	1.996	0.745	2.5	2.119
60	2.115	2.029	0.701	2.8	2.307

Compared with the original dimension parameters, the optimized parameters greatly improve the rotation capacity of the moving platform, which can accomplish a rotation angle of 35° about the x_b and y_b axes at each point of the task workspace. According to the design concept of the HPM, the variable θ takes the maximum value when the end-effector is in the maximum extreme position. From Table 3, we conclude that the maximum value of θ that can meet the boundary honeycombs' perfusion is 60°, which is

Table 3 Values for the parameters of the proposed HPM

θ/(°)	λ_1	λ_2	λ_3	λ_4	s_{imin}/mm	s_{imax}/mm	s_{7min}/mm	s_{7max}/mm	z_{min}/mm	z_{max}/mm
20	2.115	2.029	0.701	1.6	47.81	1327.97	934.07	1196.41	1120	1330
30	2.115	2.029	0.701	1.9	84.39	1321.67	915.00	1178.19	1330	1540
40	2.115	2.029	0.701	2.2	131.16	1328.59	917.96	1181.01	1540	1750
50	2.115	2.029	0.701	2.5	200.09	1353.27	949.24	1210.92	1750	1960
60	2.115	2.029	0.701	2.8	301.11	1402.62	1014.26	1273.31	1960	2170

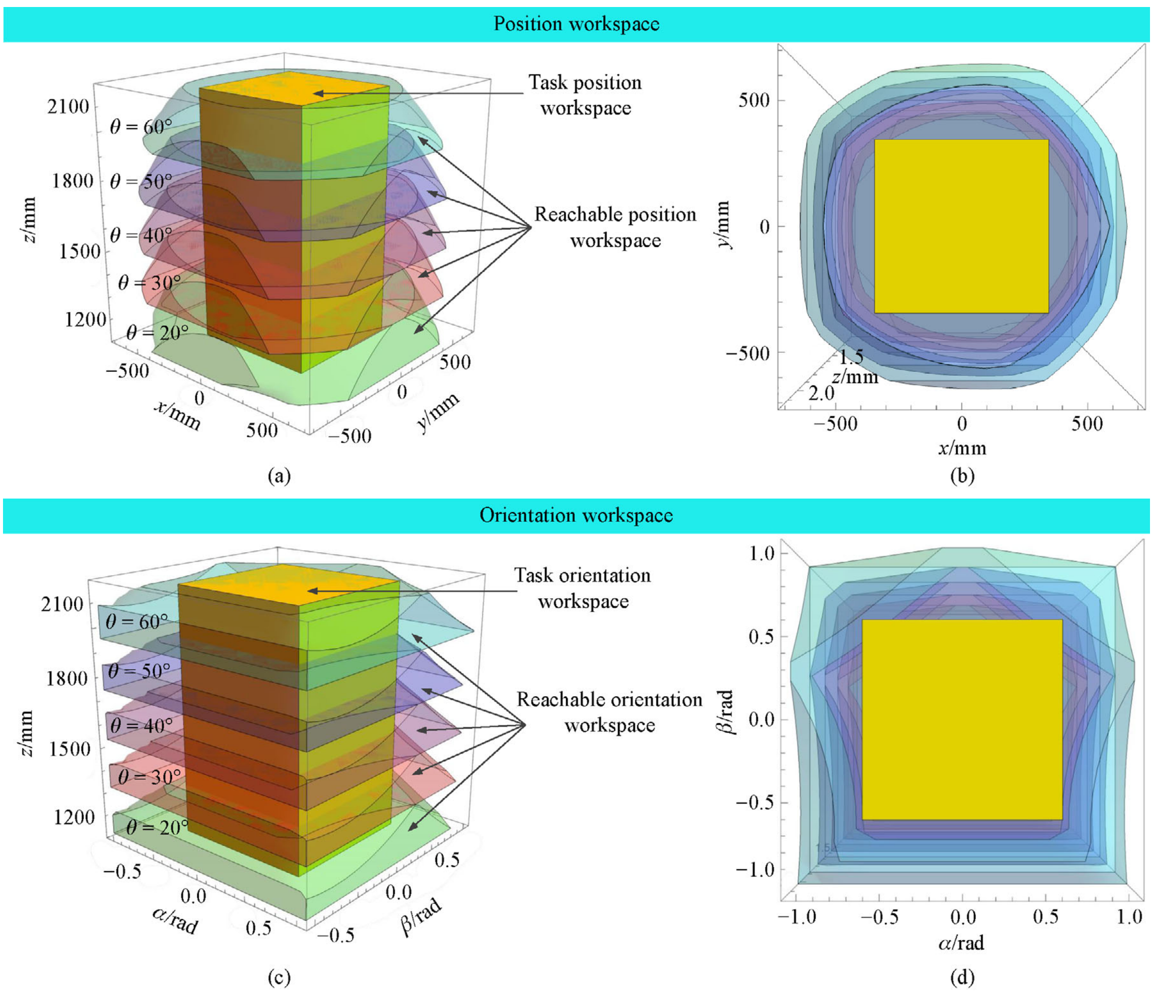

Fig. 11 Comparison of the reachable workspace and task workspace of the proposed HPM: (a) 3D and (b) top views of the comparison of the position workspace; (c) 3D and (d) top views of the comparison of the orientation workspace.

smaller than the original 75°. The small θ helps enhance the entire HPM's stiffness. Figure 11 presents the reachable workspace and task workspace of the HPM with the optimized structural parameters when the value of θ is 20°, 30°, 40°, 50°, and 60°. Figures 11(a) and 11(b) show the 3D view and top view of the reachable position workspace and task position workspace, respectively. Similarly, Figs. 11(c) and 11(d) show the 3D view and top view of the reachable orientation workspace and task orientation workspace, respectively. The reachable workspace and task workspace regions are marked with rainbow and yellow colors, respectively. These figures indicate that the reachable position workspace and reachable orientation workspace of the proposed reconfigurable HPM can satisfy task position workspace and task orientation workspace with the introduction of the reconfigurable base.

6 Conclusions

This study examines the dimensional synthesis of the 5-DOF HPM that was introduced in a previous work. On the basis of screw theory, analyses of mobility, inverse kinematics, and the Jacobian matrix are conducted. In accordance with the structural features of the HPM, the related constraints, objective function, and design variables are proposed in consideration of all the structure parameters. Afterward, dimensional synthesis of the HPM is conducted based on the given variable constraints by GA. The optimization results, including the fitness value of the objective function and the current best individual values of the variables with different values of θ, are obtained. The optimal parameters of the HPM are determined through analysis and verification.

The optimization results indicate that the perfusion platform's orientation workspace is greatly improved by the optimized structural parameters. The maximum angle of θ that can satisfy the perfusion of the boundary honeycombs is smaller than the value before optimization. This condition remarkably improves the stiffness of the proposed HPM. This research is expected to provide a theoretical foundation for subsequent error analyses and prototype fabrication.

Acknowledgements The authors gratefully acknowledge the financial support provided by the Fundamental Research Funds for Central Universities, China (Grant No. 2018JBZ007), the China Scholarship Council (Grant No. 201807090006), and the National Natural Science Foundation of China (Grant No. 51675037).

References

1. Ackerman P K, Baker, A L, Newquist C W. US Patent 5322725, 1994-6-21
2. Gogu C, Bapanapalli S K, Haftka R T, et al. Comparison of materials for an integrated thermal protection system for spacecraft reentry. Journal of Spacecraft and Rockets, 2009, 46(3): 501–513
3. Erb R B, Greenshields D H, Chauvin L T, et al. Apollo thermal-protection system development. Journal of Spacecraft and Rockets, 2015, 7(1): 839–869
4. Wu D, Zhou A, Zheng L, et al. Study on the thermal protection performance of superalloy honeycomb panels in high-speed thermal shock environments. Theoretical & Applied Mechanics Letters, 2014, 4(2): 19–26
5. Merlet J P. Parallel Robots. Dordrecht: Kluwer Academic Publishers, 2000
6. Liu Y, Wang L, Wu J, et al. A comprehensive analysis of a 3-P(Pa)S spatial parallel manipulator. Frontiers of Mechanical Engineering, 2015, 10(1): 7–19
7. Chaker A, Mlika A, Laribi M A, et al. Synthesis of spherical parallel manipulator for dexterous medical task. Frontiers of Mechanical Engineering, 2012, 7(2): 150–162
8. Dong W, Du Z, Xiao Y, et al. Development of a parallel kinematic motion simulator platform. Mechatronics, 2013, 23(1): 154–161
9. Guo S, Li D, Chen H, et al. Design and kinematic analysis of a novel flight simulator mechanism. In: Proceedings of 2014 International Conference on Intelligent Robotics and Applications (ICIRA). Guangzhou: Springer, 2014, 23–34
10. Wu G, Bai S, Hjørnet P. Architecture optimization of a parallel Schönflies-motion robot for pick-and-place applications in a predefined workspace. Mechanism and Machine Theory, 2016, 106: 148–165
11. Mo J, Shao Z, Guan L, et al. Dynamic performance analysis of the X4 high-speed pick-and-place parallel robot. Robotics and Computer-Integrated Manufacturing, 2017, 46: 48–57
12. Wu J, Gao Y, Zhang B, et al. Workspace and dynamic performance evaluation of the parallel manipulators in a spray-painting equipment. Robotics and Computer-Integrated Manufacturing, 2017, 44: 199–207
13. Zhang B, Wu J, Wang L, et al. Accurate dynamic modeling and control parameters design of an industrial hybrid spray-painting robot. Robotics and Computer-Integrated Manufacturing, 2020, 63: 101923
14. Xie F, Liu X, Wang J A. 3-DOF parallel manufacturing module and its kinematic optimization. Robotics and Computer-Integrated Manufacturing, 2012, 28(3): 334–343
15. Sun T, Song Y, Dong G, et al. Optimal design of a parallel mechanism with three rotational degrees of freedom. Robotics and Computer-Integrated Manufacturing, 2012, 28(4): 500–508
16. Yang H, Fang H, Ge Q J, et al. On the kinematic performance of a novel 5-DOF reconfigurable hybrid manipulator with ultra large workspace for automatic perfusion of a large-scale spherical honeycomb structure. In: Proceedings of 2019 ASME International Design Engineering Technical Conferences (IDETC). Anaheim: ASME, 2019, 1–9
17. Liu X. Optimal kinematic design of a three translational DoFs parallel manipulator. Robotica, 2006, 24(2): 239–250
18. Liu X, Li J, Zhou Y. Kinematic optimal design of a 2-degree-of-freedom 3-parallelogram planar parallel manipulator. Mechanism and Machine Theory, 2015, 87: 1–17
19. Liu X, Chen X, Li Z. Modular design of typical rigid links in parallel

kinematic machines: Classification and topology optimization. Frontiers of Mechanical Engineering, 2012, 7(2): 199–209
20. Shin H, Lee S, Jeong J I, et al. Antagonistic stiffness optimization of redundantly actuated parallel manipulators in a predefined workspace. IEEE/ASME Transactions on Mechatronics, 2013, 18(3): 1161–1169
21. Liu X, Wang J. A new methodology for optimal kinematic design of parallel mechanisms. Mechanism and Machine Theory, 2007, 42(9): 1210–1224
22. Wang L, Xu H, Guan L. Optimal design of a 3-PUU parallel mechanism with 2R1T DOFs. Mechanism and Machine Theory, 2017, 114: 190–203
23. Kelaiaia R, Company O, Zaatri A. Multiobjective optimization of a linear Delta parallel robot. Mechanism and Machine Theory, 2012, 50: 159–178
24. Wan X, Li Q, Wang K. Dimensional synthesis of a robotized cell of support fixture. Robotics and Computer-Integrated Manufacturing, 2017, 48: 80–92
25. Altuzarra O, Pinto C, Sandru B, et al. Optimal dimensioning for parallel manipulators: Workspace, dexterity, and energy. Journal of Mechanical Design, 2011, 133(4): 041007
26. Wu J, Chen X, Li T, et al. Optimal design of a 2-DOF parallel manipulator with actuation redundancy considering kinematics and natural frequency. Robotics and Computer-Integrated Manufacturing, 2013, 29(1): 80–85
27. Qi Y, Sun T, Song Y. Multi-objective optimization of parallel tracking mechanism considering parameter uncertainty. Journal of Mechanisms and Robotics, 2018, 10(4): 041006
28. Klein J, Spencer S, Allington J, et al. Optimization of a parallel shoulder mechanism to achieve a high-force, low-mass, robotic-arm exoskeleton. IEEE Transactions on Robotics, 2010, 26(4): 710–715
29. Song Y, Lian B, Sun T, et al. A novel five-degree-of-freedom parallel manipulator and its kinematic optimization. Journal of Mechanisms and Robotics, 2014, 6(4): 041008
30. Cheng Y, Yu D. Optimal design of a parallel bionic eye mechanism. Journal of Mechanisms and Robotics, 2019, 33(2): 879–887
31. Daneshmand M, Saadatzi M H, Kaloorazi M H F, et al. Optimal design of a spherical parallel manipulator based on kinetostatic performance using evolutionary techniques. Journal of Mechanical Science and Technology, 2016, 30(3): 1323–1331
32. Gosselin C, Angeles J. A global performance index for the kinematic optimization of robotic manipulators. Journal of Mechanical Design, 1991, 113(3): 220–226
33. Huang T, Li M, Zhao X, et al. Conceptual design and dimensional synthesis for a 3-DOF module of the TriVariant—A novel 5-DOF reconfigurable hybrid robot. IEEE Transactions on Robotics, 2005, 21(3): 449–456
34. Liu H, Huang T, Mei J, et al. Kinematic design of a 5-DOF hybrid robot with large workspace/limb–stroke ratio. Journal of Mechanical Design, 2007, 129(5): 530–537
35. Sun T, Song Y, Li Y, et al. Workspace decomposition based dimensional synthesis of a novel hybrid reconfigurable robot. Journal of Mechanisms and Robotics, 2010, 2(3): 031009
36. Fang Y, Tsai L W. Structure synthesis of a class of 4-DoF and 5-DoF parallel manipulators with identical limb structures. International Journal of Robotics Research, 2002, 21(9): 799–810
37. Joshi S A, Tsai L W. Jacobian analysis of limited-DOF parallel manipulators. Journal of Mechanical Design, 2002, 124(2): 254–258
38. Angeles J. The design of isotropic manipulator architectures in the presence of redundancies. International Journal of Robotics Research, 1992, 11(3): 196–201